Nanoscale

PAPER

View Article Online
View Journal | View Issue

Cite this: *Nanoscale*, 2024, **16**, 4105

Manipulating ultrafast magnetization dynamics of ferromagnets using the odd–even layer dependence of two-dimensional transition metal di-chalcogenides†

Soma Dutta, [a] Sajid Husain,*‡[b] Prabhat Kumar, [c] Nanhe Kumar Gupta,[d] Sujeet Chaudhary,[d] Peter Svedlindh[b] and Anjan Barman *[a]

Two-dimensional transition metal dichalcogenides (TMDs) have drawn immense interest due to their strong spin–orbit coupling and unique layer number dependence in response to spin–valley coupling. This leads to the possibility of controlling the spin degree of freedom of the ferromagnet (FM) in thin film heterostructures and may prove to be of interest for next-generation spin-based devices. Here, we experimentally demonstrate the odd–even layer dependence of WS_2 nanolayers by measurements of the ultrafast magnetization dynamics in WS_2/Co_3FeB thin film heterostructures by using time-resolved Kerr magnetometry. The fluence (photon energy per unit area) dependent magnetic damping (α) reveals the existence of broken symmetry and the dominance of inter- and intraband scattering for odd and even layers of WS_2, respectively. The higher demagnetization time, τ_m, in 3 and 5 layers of WS_2 is indicative of the interaction between spin–orbit and spin-valley coupling due to the broken symmetry. The lower τ_m in even layers as compared to the bare FM layer suggests the presence of a spin transport. By correlating τ_m and α, we pinpointed the dominant mechanisms of ultrafast demagnetization. The mechanism changes from spin transport to spin-flip scattering for even layers of WS_2 with increasing fluence. A fundamental understanding of the two-dimensional material and its odd–even layer dependence at ultrashort time-scales provides valuable information for designing next-generation spin-based devices.

Received 5th December 2023,
Accepted 25th January 2024

DOI: 10.1039/d3nr06197c

rsc.li/nanoscale

Introduction

Despite countless fascinating characteristics of graphene, the lack of intrinsic spin–orbit coupling in graphene has led to the discovery of two-dimensional (2D) transition metal dichalcogenides (TMDs) MX_2, where M is a transition metal and X is a chalcogen atom. Different TMDs have rapidly emerged during the last decade due to their potential for a wide range of applications and rich physics. Among them, group-VI TMDs (M = W, Mo and X = S, Se, Te) have shown unique electronic band structure properties depending on the layer number.[1–4] A monolayer (ML) of a TMD corresponds to half a unit cell of the bulk crystal, implying that the mirror inversion symmetry is broken in odd numbers of layers. The top of the valence band and the bottom of the conduction band consist of two inequivalent Q valleys in addition to the splitting at K and K′ points of the hexagonal Brillouin zone[2] in TMDs. Due to the lack of inversion symmetry in odd numbers of layers, the charges on the M and X atoms generate local in-plane electric fields and cause spin–orbit interaction which is strong enough to orient the spins in the bands perpendicular to the ML. Thus, this effect imitates a perpendicular magnetic field causing a giant Zeeman splitting of valleys that become fully spin polarized.[5] Based on the possibility to manipulate this valley degree of freedom, the concept of valleytronics[6] has emerged providing alongside the spin–orbit coupling (SOC) due to the d orbitals of the heavy metal atom, a way for spin manipulation. These effects lead to spin and valley coupled physics (spin–valleytronics), such as the valley Hall effect accompanied by the spin

[a]*Department of Condensed Matter and Materials Physics, S. N. Bose National Centre for Basic Sciences, Block JD, Sector-III, Salt Lake, Kolkata 700 106, India. E-mail: abarman@bose.res.in*
[b]*Department of Materials Science and Engineering, Uppsala University, Box 35, SE-751 03 Uppsala, Sweden. E-mail: shusain@lbl.gov*
[c]*Department of Thin Films and Nanostructures, Institute of Physics of the Czech Academy of Sciences, Cukrovarnická 10/112, 162 00 Prague, Czech Republic*
[d]*Thin Film Laboratory, Department of Physics, Indian Institute of Technology Delhi, New Delhi 110016, India*
†Electronic supplementary information (ESI) available. See DOI: **https://doi.org/10.1039/d3nr06197c**
‡Present address: Materials Sciences Division, Lawrence Berkeley National Laboratory, CA 94720, USA.

Hall effect,[7,8] suppression of spin and valley relaxation,[9] *etc*. Rather than the widely used electrical[10,11] and magnetic[12] methods, joint theory–experiment reports have shown that the spin–valley polarization and intervalley coupling of excitonic states in different valleys can be accessible through optical excitation.[13] Several theoretical[9,14] and experimental[15] reports have drawn attention to the combination of 2D TMDs with strong SOC with a 3d ferromagnet (FM) to modify the magnetic properties of the FM layer and to promote layer number dependent properties of the heterostructure.[16] This layer number dependence is one of the unique characteristics of TMDs, which is however not yet been fully explored. Thus, it is essential to carry out a comprehensive study of the magnetization dynamics (*via* optical excitation) at ultrafast timescales of the layered TMDs as a function of the layer number. Previous reports suggest that the strong SOC promotes transfer of spin angular momentum within the spin system and plays an important role in manipulating the ultrafast demagnetization time (τ_m), spin switching and spin-wave propagation.[16–20]

An all-optical study of magnetization dynamics using a pump-probe technique based on time-resolved magneto-optical Kerr effect (TR-MOKE) microscopy is one of the best methods that can provide a detailed understanding of the effect of TMD materials on a FM at the time scale of one billionth of a second[20] and magnetization precession associated with damping from picoseconds to a sub-nanosecond timescale. Due to broken inversion symmetry,[21] interband optical transitions will have a strong impact on magnetic damping[22] *vis-à-vis* ultrafast demagnetization. During the optical excitation in TMDs, valley dependent charge[23] transfer is the mechanism underpinning all-optical switching (AOS)[24] and hence ultrafast demagnetization. However, the microscopic mechanism and the role of spin–valley coupling have not been studied in detail for TMD based heterostructures.

In this work, we report the fluence dependent ultrafast demagnetization (τ_m) and damping (α) in WS_2 (n_{ML} = 0, 1, 2, 3, 4, 5)/Co_3FeB (6 nm)/Al (4 nm) thin film heterostructures by using the all-optical TR-MOKE technique. Compared to other TMDs, WS_2 has high spin–orbit coupling, better thermal stability, and high field effect mobility.[25] Its foremost stability with strong in-plane bonds and ability to form hybrid interfaces without any lattice matching make it a potential 2D material for magnetic information storage at an atomically thin limit. From the modulation of damping with pump laser fluence for different WS_2 layer numbers, it is observed that the broken inversion symmetry for odd numbers of layers leads to interband transitions, whereas even layers are governed by intraband transitions. We have extracted the dominant contributions for ultrafast demagnetization by correlating τ_m and α. In the case of n_{ML} = 0 (bare FM layer), both the ultrafast demagnetization and damping are governed by the spin-flip scattering (SFS) of the 3d itinerant electrons by impurities or quasiparticles. For odd number of layers, SFS dominates for the entire fluence range, while for even number of WS_2 layers, spin pumping dominates at low fluences but with the increase of laser fluence, SFS overshadows spin pumping. This study provides a detailed understanding of the magnetization dynamics and enables a non-volatile control of the ultrafast relaxation based on the layer number.

Experimental details

Controlled WS_2 layers were prepared by the combined process of ion beam sputtering and subsequent plasma sulphurization of W films on thermally oxidized Si substrates. A detailed sulphurization recipe can be found in other reports.[26] After the growth of the WS_2 films, the samples were transferred back to the ion beam sputtering chamber for the growth of 6 nm-thick Co_3FeB thin films at room temperature. The details related to the deposition of Co_3FeB can be found in a previous report.[22] Following that a 4 nm-thick Al layer was deposited as a capping layer to prevent the surface from degradation. Thus, the heterostructure stacks consist of the following layers from the bottom to the top: Sub//WS_2 (n_{ML} = 0,1,2,3,4,5)/Co_3FeB (6 nm)/Al (4 nm), where the nominal thicknesses are given in parentheses. For simplicity, the heterostructures are described as WS_2 (n_{ML})/Co_3FeB throughout the manuscript. The film thickness and roughness were obtained by X-ray reflectivity (XRR) measurements and a ML of WS_2 corresponding to ~9 Å thickness and WS_2 layer numbers are confirmed by Raman spectroscopy as shown in the ESI.†

The static magnetic properties (see the ESI†) of the samples were measured using a vibrating sample magnetometer (VSM), whereas the magnetization dynamics were investigated using a two colour non-collinear pump-probe based TR-MOKE technique. The TR-MOKE setup consists of a femtosecond regenerative amplified laser system with a central wavelength of 800 nm, a pulse width of ~35 fs and a repetition rate of 1 kHz. A part of this fundamental laser beam is passed through a second harmonic generator to double its frequency and generate a pump laser of wavelength 400 nm, with a pulse width of >35 fs with an identical repetition rate. The magnetization dynamics is excited by an intense pump beam (fluence between 2.5 and 15 mJ cm^{-2}) whereas a small part of the rest of the fundamental laser beam (fluence of 1 mJ cm^{-2}) is used as a probe beam to measure the magnetization dynamics by detecting the transient Kerr rotation signal. In our TR-MOKE experiment, the pump beam is incident at a 45° angle to the sample plane and focused on a spot having a diameter of ~250 μm. The probe beam is tightly focused on a spot of diameter ~100 μm and is incident normally on the sample plane located at the centre of the pump spot to detect the dynamics only from a uniformly excited region of the sample. The probe beam is polarized and chopped at a frequency of 373 Hz using an optical chopper right before reaching the sample. The transient Kerr rotation is detected in the probe beam through an analyzer and a Si detector by using a lock-in amplifier in a phase sensitive manner. The output frequency from the optical chopper is used as the reference frequency for the lock-in amplifier. An external magnetic field (tilted by ~10° out of the sample plane) is applied to introduce a finite out-of-plane

demagnetizing field, which is modulated by the pump beam to induce precessional dynamics in the samples.

Results and discussion

A schematic of the TR-MOKE setup is depicted in Fig. 1(a) along with the sample stack shown in Fig. 1(b). A typical laser induced time resolved magnetization dynamics is shown in Fig. 1(c) for the WS_2 (n_{ML} = 4)/Co_3FeB sample measured with a pump fluence of 10 mJ cm^{-2} under an in-plane bias magnetic field of 1.56 kOe. The applied magnetic field is large enough to reach saturation magnetization (Fig. S1†). The transient Kerr rotation drops within a sub-picosecond timescale followed by a recovery process. The ultrafast demagnetization[20] and fast remagnetization follow the expression derived from the phenomenological three-temperature model (3TM),[17]

$$\frac{-\Delta M_z}{M_z} = \left[\left\{\frac{A_1}{(t/\tau_0+1)^{\frac{1}{2}}} + \frac{A_1\tau_m - A_2\tau_e}{\tau_e - \tau_m}e^{-t/\tau_m} + \frac{A_2\tau_e - A_1\tau_e}{\tau_e - \tau_m}e^{-t/\tau_e}\right\}H(t) + A_3\delta(t)\right] \otimes G(t). \quad (1)$$

The 3TM is a thermodynamic model describing the spin fluctuations based on the energy transfer between three different subsystems: spin, electron, and lattice. Upon laser excitation, instantaneously created hot electrons are thermalized by electron–electron interactions. Shortly after that, spins also thermalize by electron–magnon interaction followed by ultrafast demagnetization. Then electron and spin start to relax by exchanging their energy with lattice *via* electron–phonon interaction. This is called the fast remagnetization time (τ_e). Here, A_1 represents the restoring value of $-\Delta M_z/M_z$ after equilibration of the different subsystems. A_2 represents the rise of the initial electron temperature, while A_3 represents the state filling effects due to the pump-probe temporal overlap, described by a Dirac delta function ($\delta(t)$). $H(t)$ is the Heaviside step function and $G(t)$ is the Gaussian laser pulse. This model is useful for analyzing the experimental data and extracting quantitative information on timescales of ultrafast demagnetization and fast remagnetization. These times depend not only on the coupling parameters but also on the thermodynamic quantities such as specific heats and temperatures of three different subsystems following three different coupled differential equations (details in the ESI†).[20]

Fast remagnetization is followed by a slow remagnetization process that occurs within a few hundreds of ps timescale. In this timescale, heat diffuses across the temperature gradient from the ferromagnet to the substrate *via* the intermediate layer, *i.e.*, WS_2, called the slow remagnetization time (τ_1). Exponentially decaying slow remagnetization superimposed

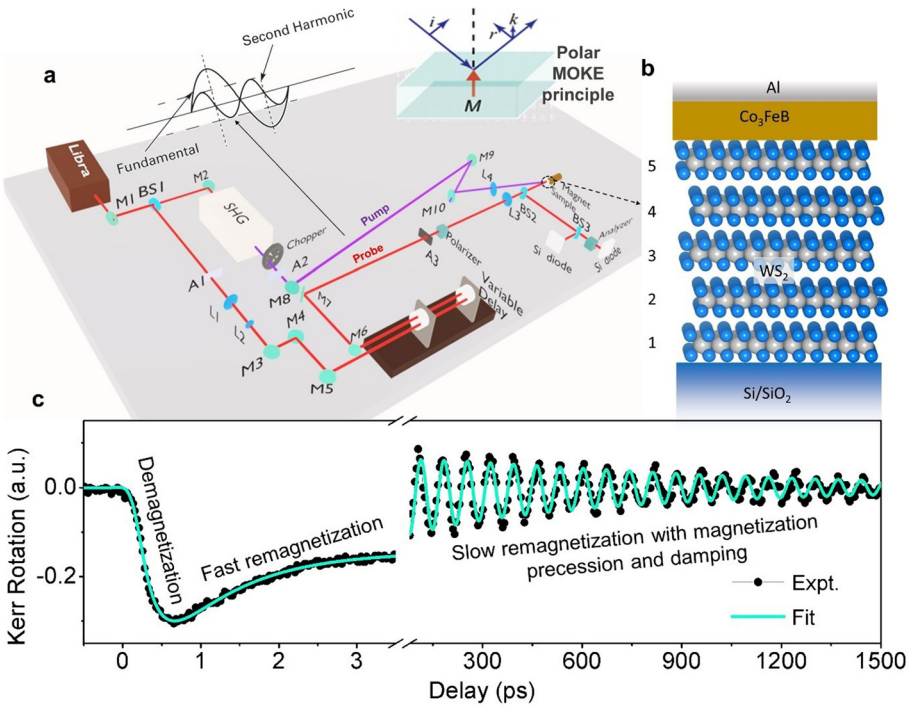

Fig. 1 (a) TR-MOKE experimental setup. (b) Layer schematic of the WS_2/Co_3FeB/Al heterostructure. (c) Recorded data on the WS_2 (n_{ML} = 4)/Co_3FeB sample at an external bias magnetic field of 1.56 kOe and a pump fluence of 10 mJ cm^{-2}. The three important temporal regimes are indicated in the graph. The black solid lines are fit to eqn (1) and (2).

with magnetization precession and damping can be fitted with an exponentially damped sinusoidal function,

$$M_z(t) = M_z(0)\left(\mathrm{Ae}^{-\left(\frac{t}{\tau_1}\right)} + \mathrm{Be}^{-\left(\frac{t}{\tau}\right)}\sin(2\pi ft + \phi)\right). \quad (2)$$

The precession frequency f is extracted from the fast Fourier transform (FFT), while the decay time τ and the initial phase of the precession ϕ are fitting parameters. The effective magnetization (M_{eff}) can be extracted by fitting the bias field (H) dependent f using Kittel's formula neglecting the anisotropy energy in amorphous Co_3FeB,[27]

$$f = \frac{\gamma}{2\pi}(H(H + 4\pi M_{\mathrm{eff}}))^{1/2}, \quad (3)$$

where $\gamma = g\mu_B/\hbar$; g, μ_B and $\hbar$ are the Landé g-factor, Bohr magneton and reduced Planck's constant, respectively. The extracted values of τ and M_{eff} from eqn (2) and (3) are used to find the effective damping parameter at a particular bias field using the expression[28]

$$\alpha_{\mathrm{eff}} = \frac{1}{\gamma\tau(H + 2\pi M_{\mathrm{eff}})}. \quad (4)$$

The magnetization precession in a magnetic field of 1.56 kOe field (Fig. 2(a)) is fitted with eqn (2) and (3) is used to fit f *vs.* H for different WS_2 (n_{ML})/Co_3FeB samples at a pump fluence of 10 mJ cm^{-2}; the results are shown in Fig. 2(b). The extracted M_{eff} values for different layer numbers of WS_2 (Fig. 2(c)) show a decreasing trend following previous results for TMD/FM heterostructures.[22,26] Here, the 5d electrons of W are strongly hybridized with the 3d electrons of Co/Fe at the interface reducing the magnetization at the interface. A finite pd hybridization between Co/Fe and S may also contribute towards reducing the effective magnetization.[26]

Using eqn (4), the effective damping parameter is calculated for the field range of ~840 Oe to ~2480 Oe (Fig. 3(a)). The magnetic damping includes both intrinsic and extrinsic contributions. Extrinsic contributions arise from magnetic inhomogeneities and TMS.[29,30] Inhomogeneities in Co_3FeB thin films may induce a variation of spin orientation *via* local magnetic anisotropy fields giving rise to a dephasing effect and an enhancement of the damping parameter when the applied field is not strong enough to align all spins.[31] TMS occurs when two spin waves interact at an impurity or discontinuity site ($k \neq 0$) in such a way that they transfer energy between the two spin waves and dissipate some of their energy at the site of the impurity. The scattering strength depends on the interfacial roughness that gives rise to an interfacial magnetic anisotropy fluctuating field leading to TMS. Thus, a strong enough applied field can suppress the extrinsic contributions.[32] For all the layers of WS_2, the effective damping (α_{eff}) decreases gradually and reaches a nearly saturated value at a higher H indicating that the inhomogeneous magnetic distribution is suppressed at large external magnetic fields. The

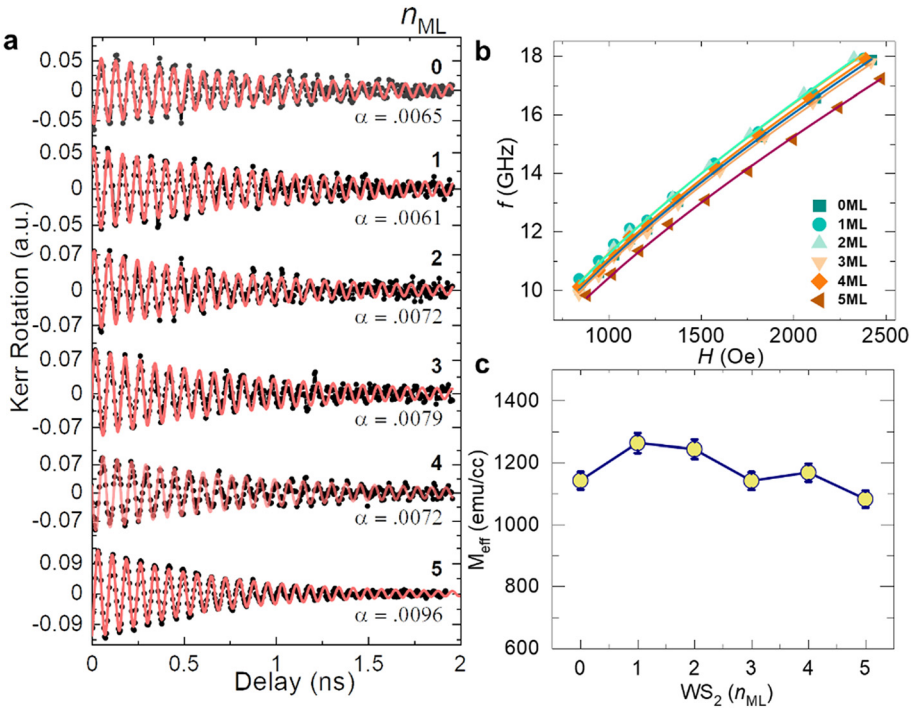

Fig. 2 (a) Time resolved Kerr rotation showing the damped magnetization precession of WS_2 (n_{ML})/Co_3FeB thin film heterostructures measured with a pump fluence of 10 mJ cm^{-2} at an external bias field of 1.56 kOe. The symbols are the experimental data points, and the solid lines are fits to eqn (2). (b) Corresponding precession frequency f of WS_2 (n_{ML})/Co_3FeB as a function of H. Solid lines are the Kittel fits. (c) Dependence of M_{eff} on the layer number of WS_2 as extracted from Kittel fits.

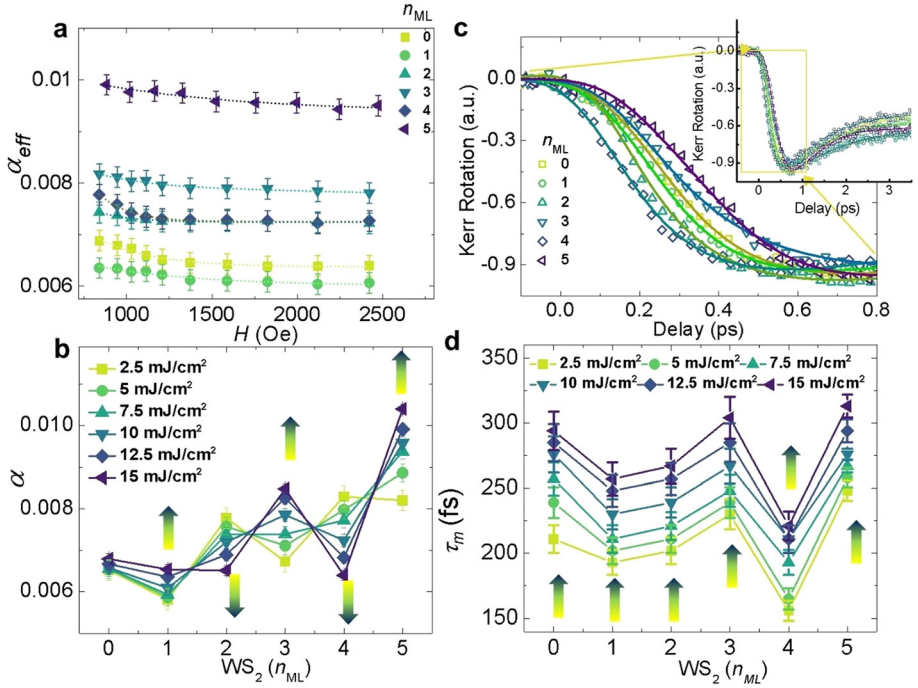

Fig. 3 (a) Dependence of the effective damping parameter α_{eff} on the magnetic field H for WS_2 (n_{ML})/Co_3FeB at a fixed pump fluence (10 mJ cm^{-2}). Dotted lines correspond to fits to exponentially decaying functions. (b) Variation of α with n_{ML} at various pump fluences (2.5–15 mJ cm^{-2}) at an external bias field of 1.56 kOe. Coloured arrows indicate the increment of fluence. (c) Ultrafast demagnetization curves of WS_2 (n_{ML})/Co_3FeB. The inset shows the time-resolved Kerr rotation over a longer time scale. Solid lines are fits to eqn (1). (d) Variation of τ_m with n_{ML} at different pump fluences (2.5–15 mJ cm^{-2}). Coloured arrows indicate the increment of fluence.

experimental data are fitted with an exponentially decaying function, $\alpha_{eff} = \alpha + \alpha_{ex}\exp(-H/H_0)$, where α corresponds to the intrinsic damping parameter and $\alpha_{ex}\exp(-H/H_0)$ is the extrinsic part of the damping.[18,33] The variation of intrinsic damping α (as the high field suppresses the extrinsic contributions) with pump fluence for WS_2 (Fig. 3(b)) shows two opposite characteristics for odd and even numbers of WS_2 layers. The gradual enhancement of the background possibly emerges from the interlayer scattering for more than 2 MLs; however, the layer number dependence is remarkable in all samples.[34]

The pump fluence increases the electronic temperature (T_e) up to thousands of Kelvins,[35] which can be related to the absorbed laser energy per unit volume (E_a) according to the following relationship:

$$E_a = C_e(T_e^2 - T_0^2)/2, \quad (5)$$

where C_e is the electronic specific heat of the sample, T_0 is the initial electronic temperature (room temperature) and E_a depends on the pump fluence as

$$E_a = F(1 - e)^{-d/\psi}(1 - R)/d, \quad (6)$$

where F is the applied pump fluence, d is the ferromagnet thickness, ψ is the optical penetration depth and R is the reflectivity of the sample. The calculated E_a and T_e are estimated in the ESI.†

In the absence of WS_2, the damping parameter is nearly constant with pump fluence for bare Co_3FeB. This is to some extent consistent with a previous study, where the damping parameter was found to be temperature independent.[36] A temperature dependent damping parameter has been reported for several FM Heusler compounds,[37,38] for which the temperature dependence is explained by inter- and intraband scattering of electrons. The interband scattering contribution enhances the damping with increasing temperature known as resistivity-like damping, while intraband scattering shows the opposite behaviour, referred to as conductivity-like damping.[39] It should be noted that the temperature dependence of the intrinsic damping is still being debated; a theoretical model[40] claims that the Gilbert damping should be independent of temperature. Thus, in a single Co_3FeB layer, we have not seen any signatures of the inter- and intraband electron scattering mechanisms. However, there is significant evidence of inter- and intraband electron scattering in the damping for the WS_2 (n_{ML} = 1, 2, 3, 4, 5)/Co_3FeB thin film heterostructures. The damping parameter increases with the increase of pump fluence for odd numbers of WS_2 layers (n_{ML} = 1, 3 and 5), indicative of interband electron scattering or resistivity-like damping, while for even numbers of WS_2 layers (n_{ML} = 2, 4), intraband electron scattering dominates.[22] According to Kambersky's spin flip scattering (SFS) mechanism, α depends on the spin–orbit coupling (SOC).[41] Furthermore, Park *et al.* have shown that for 2D materials,

the SOC strength is a function of temperature and the spin–orbit splitting factor ($\mathrm{SOC} = \frac{\hbar^2 k_0 \eta}{m^*}$, where η is the temperature dependent spin-splitting parameter).[42] Moreover, inversion symmetry breaks for 2D TMD materials with an odd number of TMD layers generating additional spin splitting. These features will provide an important implementation in spin–valleytronic devices. The layers showing higher damping would be useful for magnetic switching applications to suppress the ringing effect, while the layers with lower damping would be useful to reduce write current in STT-MRAM/SOT-MRAM devices and magnonic devices where longer propagation of spin waves is desirable. In addition to that, temperature dependent damping will provide another route to modulate damping by externally tuning the temperature of the system in place of heterostructure replacement. So, these heterostructures will be very useful to miniaturize electronic devices where temperature plays an important role.

Several mechanisms such as cooperative effects of SOC and exchange interaction,[43] SOC and applied laser field,[44] phonon mediated spin-flip scattering,[45–47] electron–magnon scattering,[48] and electron–electron scattering[49] have been suggested to explain the ultrafast demagnetization. In 2008, Malinowski *et al.* first showed that the laser induced spin transport can speed up the ultrafast demagnetization process and increase magnetic quenching in NM/FM heterostructures.[17] Local spin-flip scattering and nonlocal spin current transport are the two key mechanisms that explain ultrafast demagnetization.[50,51] An elegant method to extract the dominant contribution to ultrafast demagnetization is the simultaneous investigation and correlation of both the ultrafast demagnetization time (τ_m) and the damping parameter (α).[18,52]

The normalized ultrafast demagnetization for WS_2 (n_{ML})/Co_3FeB thin film heterostructures is shown in Fig. 3(c); the experimental results were analysed by fitting to eqn (1). Here it appears that even numbers of WS_2 (n_{ML} = 2, 4) layers reduce the demagnetization time (τ_m), indicating a spin-pumping mechanism, while odd numbers of layers enhance τ_m. This can be attributed to the broken inversion symmetry causing an extra spin-splitting in valleys for odd numbers of layers contributing to the relaxation of the spins and/or due to the uncompensated spins in the odd layer. However, a monolayer of WS_2 shows a different behaviour from the other odd numbers of layers, *i.e.*, a lower τ_m value than for the bare Co_3FeB layer. This is probably due to the absence of spin splitting in the electronic band structure in monolayer WS_2 (ref. 22). The τ_m as a function of WS_2 layer number for different pump fluences ranging from 2.5 mJ cm^{-2} to 15 mJ cm^{-2} is shown in Fig. 3(d). Unlike α, for all samples, τ_m is increasing with pump fluence due to larger spin fluctuations at elevated temperatures.[53] Variations of α and τ_m with pump fluence are shown in Fig. S4 of the ESI.† We have extracted specific heats and different coupling parameters between three different baths (electron, spin and lattice) numerically from the three-temperature modelling and tabulated in Table S2 of the ESI† for CoFeB (6 nm) thin films at different pump fluences.

Relationship between the ultrafast demagnetization time and the damping parameter: non-volatile control

The relationship between the ultrafast demagnetization time and the effective damping parameter can be used to extract the dominant microscopic mechanism behind these phenomena. The theoretical model by Koopmans *et al.*[45] predicts an inverse proportionality between τ_m and α based on Elliot-Yafet (EY)-type spin-flip scattering. Later, based on the 'breathing Fermi surface model' and the 'bubbling Fermi surface model', Fähnle *et al.*[54,55] derived both inverse and direct proportionalities between τ_m and α associated with resistivity-like and conductivity-like damping, respectively. More recently Zhang *et al.* proposed a model by incorporating spin transport through the interface of a FM/NM heterostructure[18,52] giving rise to a direct proportionality between τ_m and α when the dominating mechanism is local spin-flip scattering and an inverse proportionality when the interface spin transport dominates.

The correlation between τ_m and α is depicted in Fig. 4. In the case of odd n_{ML} (Fig. 4(a) and (b)) at the lowest and highest pump fluence used in our experiments, the results indicate a linear relationship between τ_m and α as prescribed by the breathing Fermi surface model and the Elliot-Yafet relationship,[54]

$$\tau_m = \frac{M}{\gamma p b^2 F_{el}} \alpha, \tag{7}$$

where M is the magnetization, F_{el} contains the derivatives of single-electron energies with respect to the orientation of the magnetization M, p is a material-specific parameter and b^2 is the Elliot-Yafet spin-mixing parameter. The values $\alpha/\tau_m = 4.55 \times 10^{10}$ s^{-1} and 9.24×10^{10} s^{-1} are obtained for odd numbers of layers at the lowest and highest pump fluence, respectively. At the highest fluence, even n_{ML} also indicates a linear relationship (Fig. 4(d)) and the obtained value of α/τ_m is 0.56×10^{10} s^{-1}. These values agree well with the previously reported values[16,18,55] indicating that the main governing mechanism behind the ultrafast demagnetization is the local spin-flip scattering. On the other hand, for even n_{ML} at the lowest pump fluence (Fig. 4(c)), an inverse correlation occurs,

$$\tau_m = \frac{\tilde{F}_{el}}{p b^2} \frac{1}{\alpha}, \tag{8}$$

where $\tilde{F}_{el}$ is also determined from the electronic states but is different from the F_{el}. $\tilde{F}_{el}$ can be expressed by the matrix elements formed by the two different electronic wave functions whereas F_{el} contains matrix elements formed by the same electronic wavefunctions. This indicates the dominance of spin current transport. In even n_{ML}, the absence of broken inversion symmetry causes WS_2 (n_{ML} = 2, 4)/Co_3FeB to act like a normal NM/FM heterostructure. Due to the high SOC of WS_2, it absorbs the spin angular momentum from Co_3FeB and enhances the demagnetization rate through spin-pumping.[56] The demagnetization rate $\left(\Delta\frac{1}{\tau_m} = \frac{1}{\tau_m}\Big|_t - \frac{1}{\tau_m}\Big|_{t=0}\right)$ *versus* modulation of damping ($\Delta\alpha = \alpha|_t - \alpha|_{t=0}$) at the lowest fluence for

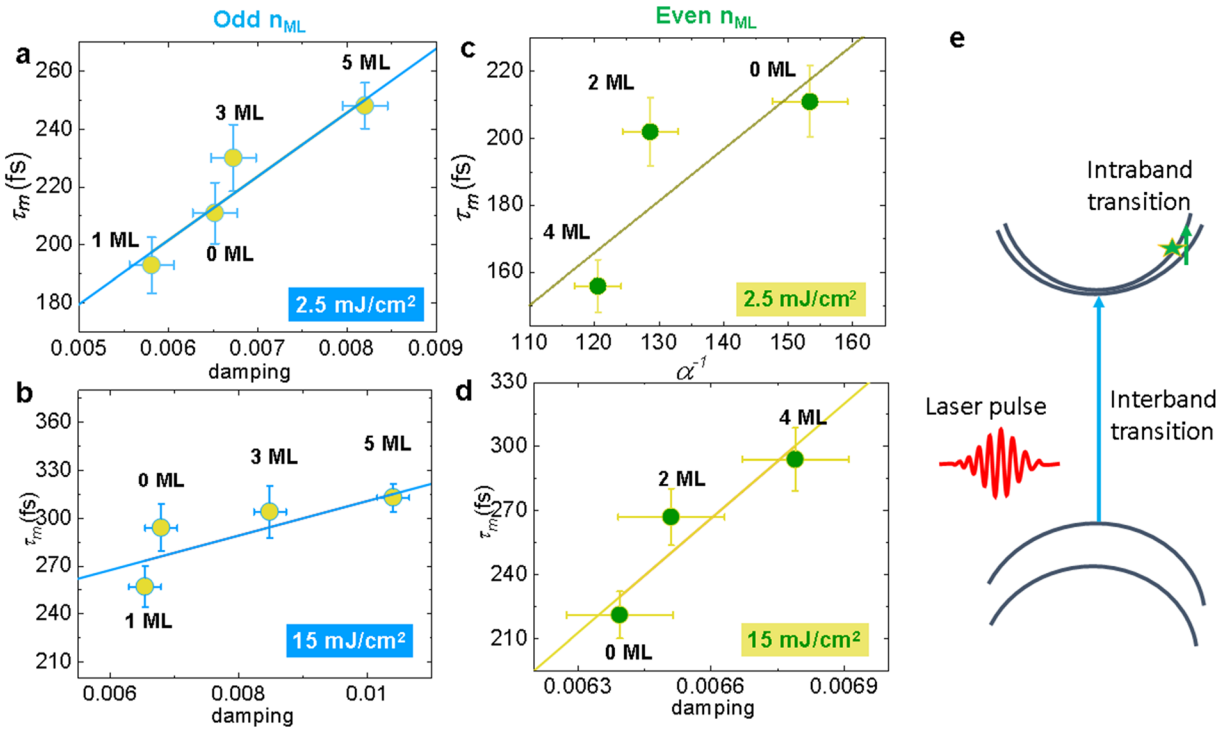

Fig. 4 Variation of τ_m as a function of α for (a and c) lowest pump fluence and (b and d) highest pump fluence for odd n_{ML} and even n_{ML}, respectively. Lines in (a), (c) and (d) are fits to eqn (7), while in (b) the line is a fit to eqn (8). (e) Cartoon of laser pulse interaction resulting in inter- and intraband transitions in WS_2.

even n_{ML} has been used to find out the spin chemical potential using the relationship,[18]

$$\Delta\frac{1}{\tau_m} = \frac{\mu_s}{\hbar}\Delta\alpha. \quad (9)$$

Here, the spin chemical potential (μ_s) quantifies the spin accumulation at the WS_2/Co_3FeB interface, which generates a spin backflow current and reduces the spin pumping. We have extracted μ_s to be 0.53 eV for even n_{ML} at low fluence, which enhances the demagnetization rate and the damping factor. This value is reasonable for a 2D material/FM heterostructure as it is in close proximity to the reported values for the graphene/CoFeB heterostructure.[57–59] This implies that with an increase in pump laser fluence, spin-flip scattering dominates over the spin pumping contribution for an even number of layers. Unlike for NM/FM heterostructures, the direct proportionality observed for odd n_{ML} is due to the interplay between the SOC and the spin–valley splitting caused by the broken inversion symmetry, which interrupts the generation and transport of spin current *via* interband transitions (Fig. 4(e)). In reciprocal space, valley separation is so large that the valley index is robust against the scattering of phonons and deformation.[60] So the effect of valley splitting on magnetization dynamics will make TMD/FM heterostructures a promising candidate for next-generation spintronic devices with high storage density and low power consumption.

Conclusions

In summary, we have systematically investigated the magnetization dynamics from femtosecond to nanosecond timescales in $WS_2(n_{ML})/Co_3FeB$ thin film heterostructures using time-resolved magneto-optical Kerr effect magnetometry. An odd–even WS_2 layer number (n_{ML}) dependence is evidenced by measurements of the damping parameter (α). The α exhibits a laser fluence dependent characteristic due to interband electron scattering in heterostructures with odd n_{ML} because of broken inversion symmetry, while in heterostructures with even n_{ML}, intraband electron scattering explains the fluence dependence. In contrast, τ_m does not show any odd–even layer dependence with fluence, confirming that electron scattering plays no significant role on femtosecond timescales. Moreover, by correlating τ_m and α, the microscopic mechanisms involved in ultrafast demagnetization have been revealed. We have found that spin current transport is generally responsible for ultrafast demagnetization at temperatures near room temperature in heterostructures with even n_{ML}. However, with an increase of pump fluence, the spin-flip scattering (SFS) starts playing a dominating role. On the other hand, in heterostructures with odd n_{ML}, the ultrafast demagnetization is dominated by the SFS mechanism for all fluences used in this study. The understanding of how the spin–valley coupling governs the odd–even layer dependence of two-dimensional materials is an important milestone for future fundamental research and applications.

Conflicts of interest

The authors declare no competing financial interest.

Acknowledgements

AB gratefully acknowledges financial assistance from the S. N. Bose National Centre for Basic Sciences (SNBNCBS), India under Project No. SNB/AB/11-12/96 and SNB/AB/18-19/211 and the Department of Science and Technology (DST), Govt. of India (Grant No. DST/NM/TUE/QM-3/2019-1C-SNB). SD acknowledges UGC, Govt of India (UGC Ref. no.: 1545/(CSIR-UGC NET JUNE 2019)) for a senior research fellowship. SH and PS acknowledge the Swedish Research Council (VR, Grant no: 2017-03799) and Carl Tryggers Stiftelse för Vetenskaplig Forskning (Grant no. CTS 17:450) for their support.

References

1 S. Husain, R. Gupta, A. Kumar, P. Kumar, N. Behera, R. Brucas, S. Chaudhary and P. Svedlindh, *Appl. Phys. Rev.*, 2020, **7**, 041312.
2 Z. Wu, S. Xu, H. Lu, A. Khamoshi, G.-B. Liu, T. Han, Y. Wu, J. Lin, G. Long, Y. He, Y. Cai, Y. Yao, F. Zhang and N. Wang, *Nat. Commun.*, 2016, **7**, 12955.
3 H. Lee, S. Deshmukh, J. Wen, V. Z. Costa, J. S. Schuder, M. Sanchez, A. S. Ichimura, E. Pop, B. Wang and A. K. M. Newaz, *ACS Appl. Mater. Interfaces*, 2019, **11**, 31543–31550.
4 P. Sarangapani, J. Charles and T. Kubis, *Phys. Rev. Appl.*, 2022, **17**, 024005.
5 A. F. Morpurgo, *Nat. Phys.*, 2013, **9**, 532–533.
6 Y. Liu, Y. Gao, S. Zhang, J. He, J. Yu and Z. Liu, *Nano Res.*, 2019, **12**, 2695–2711.
7 M. Yamamoto, Y. Shimazaki, I. V. Borzenets and S. Tarucha, *J. Phys. Soc. Jpn.*, 2015, **84**, 121006.
8 K. F. Mak, K. L. McGill, J. Park and P. L. McEuen, *Science*, 2014, **344**, 1489–1492.
9 D. Xiao, G.-B. Liu, W. Feng, X. Xu and W. Yao, *Phys. Rev. Lett.*, 2012, **108**, 196802.
10 S. Wu, J. S. Ross, G.-B. Liu, G. Aivazian, A. Jones, Z. Fei, W. Zhu, D. Xiao, W. Yao, D. Cobden and X. Xu, *Nat. Phys.*, 2013, **9**, 149–153.
11 Y. Ye, J. Xiao, H. Wang, Z. Ye, H. Zhu, M. Zhao, Y. Wang, J. Zhao, X. Yin and X. Zhang, *Nat. Nanotechnol.*, 2016, **11**, 598–602.
12 G. Aivazian, Z. Gong, A. M. Jones, R.-L. Chu, J. Yan, D. G. Mandrus, C. Zhang, D. Cobden, W. Yao and X. Xu, *Nat. Phys.*, 2015, **11**, 148–152.
13 G. Berghäuser, I. Bernal-Villamil, R. Schmidt, R. Schneider, I. Niehues, P. Erhart, S. M. de Vasconcellos, R. Bratschitsch, A. Knorr and E. Malic, *Nat. Commun.*, 2018, **9**, 971.
14 D. W. Latzke, W. Zhang, A. Suslu, T.-R. Chang, H. Lin, H.-T. Jeng, S. Tongay, J. Wu, A. Bansil and A. Lanzara, *Phys. Rev. B: Condens. Matter Mater. Phys.*, 2015, **91**, 235202.
15 G. Wu, Y. Ren, X. He, Y. Zhang, H. Xue, Z. Ji, Q. Y. Jin and Z. Zhang, *Phys. Rev. Appl.*, 2020, **13**, 024027.
16 S. Dutta, S. N. Panda, J. Sinha, S. Choudhury and A. Barman, *ACS Appl. Nano Mater.*, 2022, **5**, 17995–18003.
17 G. Malinowski, F. Dalla Longa, J. H. H. Rietjens, P. V. Paluskar, R. Huijink, H. J. M. Swagten and B. Koopmans, *Nat. Phys.*, 2008, **4**, 855–858.
18 W. Zhang, Q. Liu, Z. Yuan, K. Xia, W. He, Q.-F. Zhan, X.-Q. Zhang and Z.-H. Cheng, *Phys. Rev. B*, 2019, **100**, 104412.
19 W.-T. Lu and Z. Yuan, *Phys. Rev. B*, 2021, **104**, 214404.
20 E. Beaurepaire, J. C. Merle, A. Daunois and J. Y. Bigot, *Phys. Rev. Lett.*, 1996, **76**, 4250–4253.
21 W. Yao, D. Xiao and Q. Niu, *Phys. Rev. B: Condens. Matter Mater. Phys.*, 2008, **77**, 235406.
22 S. Husain, S. Pal, X. Chen, P. Kumar, A. Kumar, A. K. Mondal, N. Behera, N. K. Gupta, S. Hait, R. Gupta, R. Brucas, B. Sanyal, A. Barman, S. Chaudhary and P. Svedlindh, *Phys. Rev. B*, 2022, **105**, 064422.
23 Interfacial charge transfer is essential for AOS. Linearly polarized excitation should generate a coherent superposition of excitons in both K valleys. Electron hopping from a TMD to a FM is only allowed when the spin orientation of the electrons in the TMD is the same as that of the lowest-energy unoccupied conduction band. Immediately after optical excitation and before demagnetization, the transfer of electrons from the TMD with spin parallel to the FM will begin, leaving the electrons with spin opposite to that of the FM in the other K valley. However, there will be an imbalance of the remaining electrons in the K valleys. The transfer of the remaining electrons will induce remagnetization of the FM. The initial charge transfer for one of the valleys is expected to begin from a few fs to sub-hundreds of the fs timescale, before the demagnetization of the FM.
24 M. Dąbrowski, S. Guo, M. Strungaru, P. S. Keatley, F. Withers, E. J. G. Santos and R. J. Hicken, *Nat. Commun.*, 2022, **13**, 5976.
25 A. S. Sethulekshmi, J. S. Jayan, A. Saritha and K. Joseph, *J. Alloys Compd.*, 2021, **876**, 160107.
26 S. Husain, A. Kumar, P. Kumar, A. Kumar, V. Barwal, N. Behera, S. Choudhary, P. Svedlindh and S. Chaudhary, *Phys. Rev. B*, 2018, **98**, 180404.
27 H. C. Yuan, S. H. Nie, T. P. Ma, Z. Zhang, Z. Zheng, Z. H. Chen, Y. Z. Wu, J. H. Zhao, H. B. Zhao and L. Y. Chen, *Appl. Phys. Lett.*, 2014, **105**, 072413.
28 J. Walowski, M. D. Kaufmann, B. Lenk, C. Hamann, J. McCord and M. Münzenberg, *J. Phys. D: Appl. Phys.*, 2008, **41**, 164016.
29 A. Capua, S.-H. Yang, T. Phung and S. S. P. Parkin, *Phys. Rev. B: Condens. Matter Mater. Phys.*, 2015, **92**, 224402.
30 Y. Sun, H. Chang, M. Kabatek, Y.-Y. Song, Z. Wang, M. Jantz, W. Schneider, M. Wu, E. Montoya, B. Kardasz, B. Heinrich, S. G. E. te Velthuis, H. Schultheiss and A. Hoffmann, *Phys. Rev. Lett.*, 2013, **111**, 106601.

31 Y. Fan, X. Ma, F. Fang, J. Zhu, Q. Li, T. P. Ma, Y. Z. Wu, Z. H. Chen, H. B. Zhao and G. Lüpke, *Phys. Rev. B: Condens. Matter Mater. Phys.*, 2014, **89**, 094428.
32 H. Song, K.-D. Lee, C.-Y. You, S.-H. Yang, S. Parkin, B.-G. Park, J.-W. Sohn, J.-I. Hong and S.-C. Shin, *Appl. Phys. Express*, 2015, **8**, 053002.
33 X. Ma, L. Ma, P. He, H. B. Zhao, S. M. Zhou and G. Lüpke, *Phys. Rev. B: Condens. Matter Mater. Phys.*, 2015, **91**, 014438.
34 Y. Jiang, S. Chen, W. Zheng, B. Zheng and A. Pan, *Light: Sci. Appl.*, 2021, **10**, 72.
35 S. Mondal and A. Barman, *Phys. Rev. Appl.*, 2018, **10**, 054037.
36 A. Okada, S. He, B. Gu, S. Kanai, A. Soumyanarayanan, S. T. Lim, M. Tran, M. Mori, S. Maekawa, F. Matsukura, H. Ohno and C. Panagopoulos, *Proc. Natl. Acad. Sci. U. S. A.*, 2017, **114**, 3815–3820.
37 A. Kumar, F. Pan, S. Husain, S. Akansel, R. Brucas, L. Bergqvist, S. Chaudhary and P. Svedlindh, *Phys. Rev. B*, 2017, **96**, 224425.
38 B. Khodadadi, A. Rai, A. Sapkota, A. Srivastava, B. Nepal, Y. Lim, D. A. Smith, C. Mewes, S. Budhathoki, A. J. Hauser, M. Gao, J.-F. Li, D. D. Viehland, Z. Jiang, J. J. Heremans, P. V. Balachandran, T. Mewes and S. Emori, *Phys. Rev. Lett.*, 2020, **124**, 157201.
39 K. Gilmore, Y. U. Idzerda and M. D. Stiles, *Phys. Rev. Lett.*, 2007, **99**, 027204.
40 A. T. Costa and R. B. Muniz, *Phys. Rev. B: Condens. Matter Mater. Phys.*, 2015, **92**, 014419.
41 V. Kamberský, *Can. J. Phys.*, 1970, **48**, 2906–2911.
42 Y. H. Park, H. C. Koo, K. H. Kim, H. J. Kim, J. Chang, S. H. Han and H. Kim, *IEEE Trans. Magn.*, 2010, **46**, 1562–1564.
43 W. Hübner and G. P. Zhang, *Phys. Rev. B: Condens. Matter Mater. Phys.*, 1998, **58**, R5920–R5923.
44 G. P. Zhang and W. Hübner, *Phys. Rev. Lett.*, 2000, **85**, 3025–3028.
45 B. Koopmans, J. J. M. Ruigrok, F. Dalla Longa and W. J. M. de Jonge, *Phys. Rev. Lett.*, 2005, **95**, 267207.
46 B. Koopmans, G. Malinowski, F. Dalla Longa, D. Steiauf, M. Fähnle, T. Roth, M. Cinchetti and M. Aeschlimann, *Nat. Mater.*, 2010, **9**, 259–265.
47 C. Illg, M. Haag and M. Fähnle, *Phys. Rev. B: Condens. Matter Mater. Phys.*, 2013, **88**, 214404.
48 E. Carpene, E. Mancini, C. Dallera, M. Brenna, E. Puppin and S. De Silvestri, *Phys. Rev. B: Condens. Matter Mater. Phys.*, 2008, **78**, 174422.
49 M. Krauß, T. Roth, S. Alebrand, D. Steil, M. Cinchetti, M. Aeschlimann and H. C. Schneider, *Phys. Rev. B: Condens. Matter Mater. Phys.*, 2009, **80**, 180407(R).
50 A. J. Schellekens, W. Verhoeven, T. N. Vader and B. Koopmans, *Appl. Phys. Lett.*, 2013, **102**, 252408.
51 A. Eschenlohr, M. Battiato, P. Maldonado, N. Pontius, T. Kachel, K. Holldack, R. Mitzner, A. Föhlisch, P. M. Oppeneer and C. Stamm, *Nat. Mater.*, 2013, **12**, 332–336.
52 W. Zhang, W. He, X.-Q. Zhang, Z.-H. Cheng, J. Teng and M. Fähnle, *Phys. Rev. B*, 2017, **96**, 220415.
53 K. C. Kuiper, T. Roth, A. J. Schellekens, O. Schmitt, B. Koopmans, M. Cinchetti and M. Aeschlimann, *Appl. Phys. Lett.*, 2014, **105**, 202402.
54 M. Fähnle, J. Seib and C. Illg, *Phys. Rev. B: Condens. Matter Mater. Phys.*, 2010, **82**, 144405.
55 M. Fähnle and C. Illg, *J. Phys.: Condens. Matter*, 2011, **23**, 493201.
56 Y. Tserkovnyak, A. Brataas and G. E. W. Bauer, *Phys. Rev. B: Condens. Matter Mater. Phys.*, 2002, **66**, 224403.
57 S. N. Panda, S. Majumder, S. Choudhury, A. Bhattacharya, S. Sinha and A. Barman, *Nanoscale*, 2021, **13**, 13709–13718.
58 J. C. W. Song, M. S. Rudner, C. M. Marcus and L. S. Levitov, *Nano Lett.*, 2011, **11**, 4688–4692.
59 M. Massicotte, G. Soavi, A. Principi and K.-J. Tielrooij, *Nanoscale*, 2021, **13**, 8376–8411.
60 Q. Cui, Y. Zhu, J. Liang, P. Cui and H. Yang, *Phys. Rev. B*, 2021, **103**, 085421.